5-2019

Micro-CT-Based Approaches for Quantifying the Morphology of Pulverized Char Particles

Scott Jorgensen
Marquette University

Simcha L. Singer
Marquette University, simcha.singer@marquette.edu

Energy & Fuels, Vol. 33, No. 6 (2019): 4826-4834. DOI.

Micro-CT-Based Approaches for Quantifying the Morphology of Pulverized Car Particles

Scott Jorgensen
Department of Mechanical Engineering, Marquette University, Milwaukee, WI
Simcha Singer
Department of Mechanical Engineering, Marquette University, Milwaukee, WI

Abstract

Morphological analysis of pulverized coal char particles using two-dimensional (2-D) cross-sectional imaging has been widely employed, but its accuracy has not been adequately assessed. In this study, pulverized coal char particles are imaged in three dimensions (3-D) using high-resolution X-ray microcomputed tomography (micro-CT). Particle volume, macropore volume, and macroporosity are measured in three dimensions and analyzed as a function of distance from the particle center using averaging at each radial location. A technique for extracting each particle's average wall thickness, another morphological parameter used for classification, is also presented based on micro-CT imaging. When applied to pulverized bituminous coal char particles, the micro-CT-based analysis revealed a similar spatial distribution of macroporosity among a population that would typically be classified as containing both group II (mixed porous-solid) and group III (dense) particles. Wall thicknesses

determined by micro-CT were generally well predicted by a model representing the particles as thick- and thin-walled cenospheres. Comparisons between 2-D and 3-D techniques reveal significant differences because of the use of just a single cross-sectional image in 2-D approaches. A new method for estimating macroporosity from 2-D imaging, called the cylindrical stacking method, is proposed for cases in which the micro-CT analysis is not feasible.

1. Introduction

Combustion and gasification of pulverized coal are widely used for electricity generation and the production of chemicals. Because devolatilization occurs on a faster time-scale than char consumption, the latter is the overall rate-limiting process. Char particle combustion and gasification often occur under internal diffusion-controlled conditions.[1] Although the vast majority of heterogeneous reaction occurs on the surface of the micro- and mesopores because of their dominant contribution to the surface area,[2,3] the morphology of larger macropores and voids affects intraparticle transport and access to reactive sites. It has been observed by Cloke et al. that char morphology (wall thickness) had a larger impact on burnout than intrinsic reactivity.[4] It has been further demonstrated that char morphology cannot be accurately represented using spherical, homogeneous particles[5] and that existing models are limited in their predictive capabilities by their primitive treatment of the char's pore structure.[6] The effects of char morphology should therefore be incorporated into particle-scale combustion models to ensure accuracy and improve their predictive power.

To integrate char morphology into particle-scale models appropriate for incorporation into reactor-scale computational fluid dynamics (CFD) codes, the distribution of char structures must be characterized. The characterization and effects of char morphology have been widely studied, and many attempts have been made to classify char structures.[7−21] These approaches typically rely on stereological image processing techniques to estimate char morphological parameters such as porosity, wall thickness, and pore size. Three broad char morphologies are often defined:[22−25] cenospheres, solid chars, and mixed porous-solid structures. Of several classification characteristics, porosity and wall thickness provide the clearest distinction between char types. For the purpose of char morphology classification, the porosity is estimated from two-dimensional (2-D) cross-sectional images of chars embedded in an epoxy resin.[3,19,20,22−31] This porosity will be termed "macroporosity" and includes all pores and voids with sizes larger than the resolution of the imaging technique. Pores smaller than the image resolution will be lumped into what appears to be the solid carbonaceous char, so the solid material will be termed "microporous solid" (although it includes micropores, mesopores, and macropores, according to the IUPAC definition[32]).

The estimation of a particle's macroporosity using 2-D cross-sectional imaging assumes that the ratio of macropore volume to particle volume (eq 1a) can be approximated by the ratio of the cross-sectional image's macropore area to the total cross-sectional area (eq 1b)

$$\varepsilon_{\text{macro-pore}} \equiv \frac{V_{\text{macro-pore}}}{V_{\text{macro-pore}} + V_{\text{micro-porous solid}}} \quad \text{(1a)}$$

$$\varepsilon_{\text{macro-pore}} \approx \frac{A_{\text{macro-pore}}}{A_{\text{macro-pore}} + A_{\text{micro-porous solid}}}$$

(1b)

This assumption is only valid if the particle is symmetric about the measured cross section, which implies that the sampled cross section coincides with a symmetry plane of the char particle. This assumption is flawed because char particles typically have no symmetry plane because of their irregular geometry. Even for perfectly spherical particles, this assumption implies that the measured cross section intersects the sphere's center. In preparing cross-sectional samples embedded in an epoxy resin, it is unlikely that the cross sections pass through the particle centers, as pointed out by Ma and Mitchell.[24] Therefore, existing techniques for measuring the char particle macroporosity require simplifying assumptions that are difficult to satisfy, leading to potential errors in macroporosity estimation and incorrect particle classification. This may, in turn, introduce errors into combustion models which rely on a proper distribution of char particle morphologies.[22−25]

In reality, char particles have nonuniform macropore and solid structures and classifying particles based on a single-cross section does not accurately represent the morphology. Even if the population of particles is large enough such that the frequency of observed char types no longer changes appreciably with increasing population size,[27] this does not imply that the frequency of char types is correct, due to potential bias. The high degree of variability in the macropore structure and the inability of a single cross section to accurately represent the particle morphology are demonstrated in Figure 1, in which two similarly sized cross sections are obtained from X-ray microcomputed tomography (micro-CT) imaging of the same coal char particle. It is observed that the particle appears as a cenosphere in Figure 1a and as a dense char in Figure 1b, illustrating the arbitrary nature of techniques based on 2-D imaging.

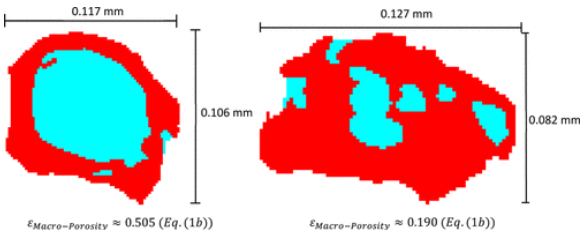

Figure 1. Two similarly sized planar slices of a single coal char particle obtained via micro-CT with estimated macroporosity from eq 1b, with microporous solid (red) and macroporosity (blue) delineated.

While quantifying char morphology using an epoxy resin cross-sectional approach has inherent drawbacks, micro-CT provides a means of circumventing these difficulties. Micro-CT enables reconstruction of the entire internal and external three-dimensional (3-D) structure of char particles, eliminating the cross-sectional selection bias associated with 2-D approaches. Micro-CT enables the analysis of volume-integrated characteristics, such as total particle volume and macroporosity, as well as characteristics, such as wall thickness, obtained via averaging over multiple 2-D cross sections. Finally, micro-CT can be used to obtain the morphology of dozens, and perhaps hundreds, of particles simultaneously and at high resolution. Mathews et al.[33] recently reviewed the application of CT to coal

for visualization of mineral and maceral dispersion, swelling, shrinking, and fracturing, but pointed out that micro-CT had never been applied to pulverized particles because of their small size.

In this paper, new approaches to characterizing char particle morphological properties based on micro-CT imaging are developed. The distribution of solid char and its macropores will be studied in three dimensions and as a function of distance from the particle center, and char wall thickness will be calculated through the use of multiple 2-D cross sections. The error associated with 2-D macroporosity estimation techniques will be quantified, and a modified 2-D technique is proposed. As a test case, the methods are applied to Illinois #6 coal char, with the data indicating that a hollow sphere morphological model may be applicable for a wide range of macroporosities.

2. Materials and Methods

2.1. Experimental and Image Analysis

The char particles used in this study were derived from Illinois #6 bituminous coal obtained from the Penn State University Coal Sample bank. On a dry basis, the coal is 13.05% ash, 40.34% volatile matter, and 46.61% fixed carbon by weight and the ultimate analysis yields 67.48% carbon, 4.82% hydrogen, 1.53% nitrogen, 4.52% sulfur, and 8.60% oxygen. Coal particles were sieved to a 105 μm nominal diameter. The particles were placed in a single layer on a sheet of aluminum foil, covered with a beaker, filled with argon and sealed. The particles were then placed in an 800 °C muffle oven for 30 s, which achieved an estimated maximum heating rate approaching 10 000 K/s. Both cenospherical and network chars were produced in roughly equal numbers. The char particles were carefully attached to a double-sided adhesive tape and mounted on a micropipette tip for micro-CT imaging. Several dozen particles were imaged at once using a GE v|tome|x s 240 X-ray micro-CT scanner, at a voltage of 80 kV, a current of 130 μA, and a resolution of 1.632 μm. The total scan time was just over 2 h. Following reconstruction, the gray-scale TIFF files were imported into Simpleware's ScanIP software for segmentation, image processing, and meshing.[34] A 3-D rendering of a char particle and its internal macropore structure is shown in Figure 2.

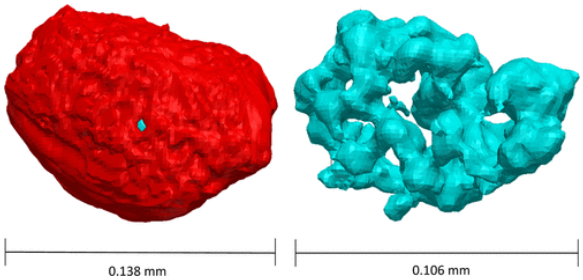

Figure 2. 3-D rendering of a char particle (red) and its internal macropore structure (blue).

A recursive Gaussian filter was applied to increase the gray-scale contrast at the boundary between the microporous char and surrounding air/macropores/voids, followed by gray-scale thresholding to differentiate the char from the surrounding air/macropores/voids. Macropores were differentiated from the surrounding fluid by segmenting between the two regions, with all void-space contained within the microporous solid border considered to be macropores. If gaps were present in the solid border separating the particle from the surrounding fluid, a curve bridging the gap was manually interpolated. This process was performed for every cross-sectional image used to construct the 3-D

particles. This avoids the use of “fill” or “close” functions that may distort the image as a whole and lead to inaccuracies in subsequent measurements.[27] Macropores thus included dead end and through pores as well as major concavities in the particle’s surface, consistent with IUPAC standards.[32] The adhesive and microporous solid had similar absorptances, but the slight gray-scale difference was sufficient to differentiate between the two materials. Although the high-resolution micro-CT was able to differentiate microporous char from resolved mineral inclusions, in the present analysis, we have only segmented solids from the resolved macropores and voids.

Figure 3a shows a gray-scale image following image processing, whereas Figure 3b shows the same cross-sectional image following segmentation. Each pixel in Figure 3 has a unit length equal to 1.632 µm. Fifty nonconjoined char particles were produced, imaged, and segmented using this process, and particles with macroporosities between 10 and 60% were analyzed.

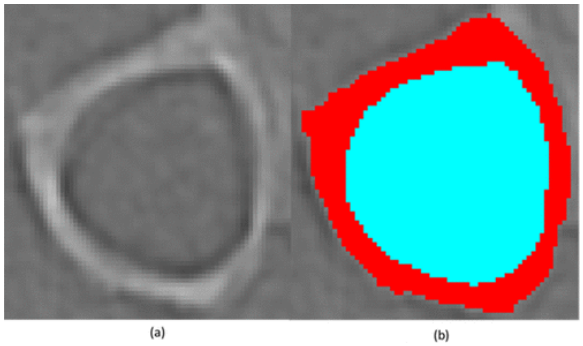

Figure 3. Cross-sectional micro-CT images of Illinois #6 coal char: (a) gray-scale image after filtering, and (b) segmented image with microporous solid shown in red and macropore region in blue.

2.2. Morphological Analysis

2.2.1. Solid Volume, Macropore Volume, and Particle Volume

Similar to the 2-D mass distribution employed by Alvarez,[3,19] volume distributions are obtained from the micro-CT image analysis and used to characterize the distribution of microporous solid volume, macropore volume, and the sum of these two volumes within the char particles. 3-D distributions can be collapsed to one-dimensional (1-D) radial distributions by summing over spherical shells at various radii to determine a surface fraction, $\emptyset_{j_k}$, using

$$\emptyset_{j_k} = \frac{1}{A}\sum_{i=1}^{n} \delta_{i\mathrm{ID}j}|A_i| \quad (2)$$

where *j* represents the surface fraction being measured and *k* is the radial position. Essentially, this procedure corresponds to averaging over polar and azimuthal directions at each radial location. Because radial distributions could not be generated in ScanIP, ANSYS Fluent was employed, which required the generation of a mesh. The *A* term in eq 2 represents the total surface area of the spherical shell. The summation is over all cells, *i*, on the sphere’s surface, with A_i being the surface area of an individual cell. The Kronecker delta term, $\delta_{i\mathrm{ID}j}$, in eq 2 returns a one if the mesh cell’s identifier, $\delta_{i\mathrm{ID}}$, which is assigned based on the classification from ScanIP, matches the variable to be measured, *j*. It is noted that index *j* may take values of “macropore,” “microporous solid,” and “particle,” where the latter

includes both macropore and microporous solid regions and is used to distinguish the particle and its macropores from its surroundings. The identifier of "surrounding fluid" applies to noncolored regions in Figure 3b, and the Kronecker delta function always returns zero for this cell. Once imported to ANSYS Fluent, particles were isotropically scaled to an effective diameter of 100 μm using the scale factor, R_{scale}, such that each particle has an equivalent volume.[35]

$$R_{\text{scale}} = \frac{\left(\frac{6}{\pi}\left(V_{\text{macro-pore}} + V_{\text{microporous solid}}\right)\right)^{1/3}}{100 \times 10^{-6}}$$

(3)

Isotropic scaling is a means of non-dimensionalization, which enables comparison of particles of different sizes.

To generate a radial distribution, the specified surface fraction, $\emptyset_{j_k}$, must be measured for concentric spheres over a range of radii. For this purpose, a "center" must be specified. Because particles are not perfect spheres, the "center" is defined as the particle's "center of volume," which would correspond to the center of mass if both microporous solid and macropores were assigned the same density. This is calculated in each of the three coordinate directions using eq 4, in which the summation is over all of the volume elements, V_i, in a specified direction, j, with L_{i_j} being the volume element's distance from the origin for a specified direction.

$$\text{CV}_j = \frac{\sum_{i=1}^{n} V_i L_{i_j}}{\sum_{i=1}^{n} V_i}$$

(4)

Spherical shells are then created around the center of volume, increasing each sphere's radius by 1 μm, with the outermost shell completely encapsulating the particle. Once the values of $\emptyset_{\text{particle,k}}$ are measured at each radii, the total volume of the entire particle is calculated using eq 5, by summing over all of the radii, r_k, with Δr being the radial spacing between shells.

$$V_{\text{particle}} = \sum_{k=1}^{n} 4\pi r_k^2 \times \emptyset_{\text{particle}_k} \times \Delta r$$

(5)

The estimated "particle" volume calculated from the radial distribution using eq 5 was compared to the meshed particle volume, which is taken to be the true volume. The particle volume estimation error was then determined using eq 6 and found to be, on average, 0.261%.

$$\%\ \text{Error} = \frac{\left|V_{\text{particle}_{\text{true}}} - V_{\text{particle}_{\text{measured}}}\right|}{V_{\text{particle}_{\text{true}}}} \times 100$$

(6)

The particle volume error from the estimation method requires surface fractions for all radii to be uniformly rescaled using eq 3 so that all particles once again have equal particle volumes.

2.2.2. Wall Thickness

Another metric of interest is the thickness of microporous solid regions or the “wall thickness,” which is reported as an average value because it is nonuniform throughout the particle. In this study, the reported wall thickness for a given particle incorporates two averages: the first is an average of multiple wall thickness measurements from a single cross section, followed by a second average using three orthogonal cross sections intersecting at the center of volume of the microporous solid. It is noted that the center of volume of the microporous solid is obtained from eq 4 by summing only over microporous solid volumes.

To calculate the microporous solid thickness for each cross section, the image is imported into MATLAB and measurement lines are drawn extending outward from the center of volume of the microporous solid with known angles θ. For each cross section, 100 measurement lines are drawn, as illustrated in Figure 4.

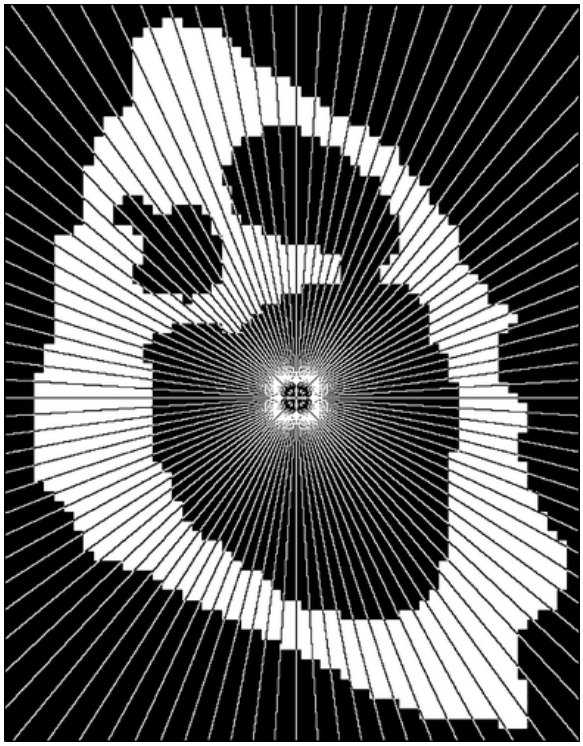

Figure 4. Microporous solid thickness measurement lines with (white) microporous solid and (black) macropores.

The microporous solid thickness, $t_{\text{microporous solid}}$, is determined by summing over all pixels falling within the measurement line. (It is noted that the pixels in the MATLAB image do not exactly correspond to the voxels/pixels obtained from micro-CT.)

$$t_{\text{micro-porous solid}} = \sum_{i}^{n_{\text{pixels}}} L_{\text{pixel}_{\text{line}_i}} \times \delta_{\text{micro-porous solid},i}$$

(7)

In eq 7, $\delta_{\text{microporous solid,i}}$ equals one when the pixel falls within the microporous solid and zero otherwise. The length of a measurement line within a particular pixel, $L_{\text{pixel}_{\text{line}_i}}$, is determined for each pixel using the location of the intersection points of the measurement line with the pixel box, as illustrated in Figure 5. The location of "intersection 2" is determined using the position of "intersection 1", the location of the pixel borders (which are always $L_{\text{pixel}}/2$ away from the pixel's center) and the angle θ which is specified for each measurement line. The length of a MATLAB pixel is L_{pixel} and is determined for each image. After averaging the 100 microporous solid thicknesses, the measurement is scaled using eq 3.

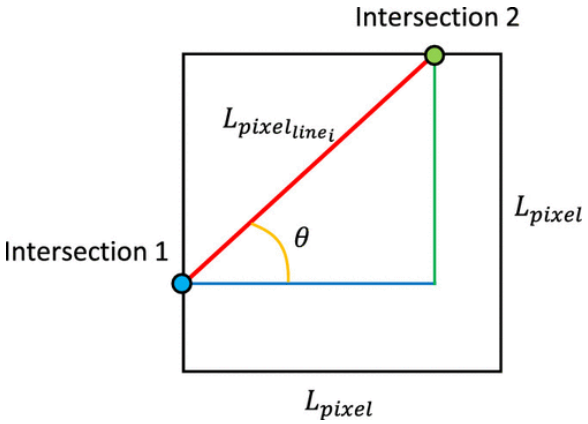

Figure 5. Determination of measurement line length within a single pixel.

Because $t_{\text{microporous solid}}$ is defined as the sum of microporous solid pixels encountered over the length of a measurement line, lines that intersect several distinct internal regions of microporous solid report the length as a single value, equal to the sum of the individual lengths. This characterization, as opposed to an average length, was chosen because it most closely corresponds to the relevant diffusion length-scale. Because diffusion through macropores occurs quickly compared to diffusion through the microporous solid, the relevant length-scale for diffusion from the particle's surface to its center is approximately equal to the sum of microporous solid thicknesses along that path.

2.2.3. Macroporosity and Comparison to 2-D Approaches

The final particle characteristic to be analyzed is the macroporosity, $\varepsilon_{\text{macropore}}$. Total macroporosity is determined in ScanIP by dividing the sum of all macropore voxels by the sum of all macropore and microporous solid voxels, which yields the macroporosity of the particle, as shown in eq 1a. Determination of this true macroporosity from 3-D imaging also allows for the assessment of 2-D cross-sectional techniques for estimating macroporosity. Furthermore, resolution of entire particles via micro-CT enables the selection of cross sections that intersect the microporous solid's center of volume, which yield the minimum error for the 2-D cross-sectional method.

The accuracy of 2-D estimation techniques can also be improved by eliminating simplifying assumptions. The assumption that the area ratio equals the volume ratio (eq 1b) can be improved upon, even in the context of 2-D approaches, by using a new technique for estimating particle macroporosity that is termed the "cylindrical stacking method." This terminology is used because only a finite height of the cross-sectional image is assumed to be symmetrical about its center of volume, rather than the entire cross section. Thus, the particle and macropore volume are modeled as stacks of short cylinders (disks) with varying diameters, as illustrated in Figure 6.

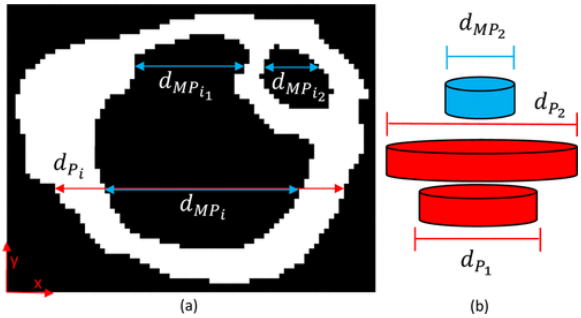

Figure 6. (a) Determination of macropore and particle diameters and (b) "stacked cylinders" for measured diameters.

The determination of the individual cylinder diameters requires measuring the length of particle and macropore regions in the *x*-direction for every row of pixels in the *y*-direction and was performed in MATLAB. The height of the cylinders is selected to be the height of a pixel (*y*-direction) in the MATLAB cross-sectional image. Two different diameters must be measured for every row of pixels: the particle diameter denoted d_{P_i} and the macropore diameter denoted d_{MP_i}, with subscript P standing for particle and subscript MP standing for macropore, as shown in Figure 6a, with corresponding cylinders shown in Figure 6b. A special case for the macropore diameter is also shown in Figure 6a, in which the macropore is divided into two regions. In such a case, the macropore diameter is defined as the sum of the individual diameters, given by

$$d_{\mathrm{MP}_i} = \sum_{j=1}^{n} d_{\mathrm{MP}_{i_j}}$$

(8)

The particle and macropore volumes are then determined by summing the volumes of each discrete cylinder up through the *n*th pixel, n_{pixel}, in the *y*-direction

$$V_{\mathrm{P}} = \sum_{i=1}^{n_{\mathrm{pixel}}} \frac{\pi}{4} {d_{\mathrm{P}_i}}^2 h$$

(9)

$$V_{\mathrm{MP}} = \sum_{i=1}^{n_{\mathrm{pixel}}} \frac{\pi}{4} {d_{\mathrm{MP}_i}}^2 h$$

(10)

The macroporosity can then be estimated using the cylindrical stacking method by dividing the sum of the macropore disk volumes by the particle disk volumes, which simplifies to eq 11, because the height of a pixel *h* is constant,

$$\varepsilon_{\mathrm{macro-porosity_{CSM}}} = \frac{\sum_{i=1}^{n_{\mathrm{pixel}}} {d_{\mathrm{MP}_i}}^2}{\sum_{i=1}^{n_{\mathrm{pixel}}} {d_{\mathrm{P}_i}}^2}$$

(11)

This method can be used to generate two macroporosity measurements for each cross-sectional image because cylinders with axes in the *x*-direction can also be employed.

3. Results and Discussion

Radial distributions will be presented for each individual particle imaged, and as average distributions for all 50 particles. Two particle bins were created based on macroporosity: particles with macroporosity greater than 40% are considered group II particles, and those with macroporosity between 10 and 40% considered group III particles, consistent with Ma and Mitchell's classification scheme.[24] Twenty-two particles were classified as group II and 28 as group III, with average macroporosities of 48.52 and 28.11%, respectively.

The particle volume is plotted in Figure 7 as a function of radius, with the volume of a perfect sphere indicated to show deviations from a particle surface fraction of unity. The volume versus radius relationship is calculated using eq 12, with V_{j_k} being the volume of specified variable, *j*, at radius, *k*.

$$V_{j_k} = 4\pi r_k^2 \times \emptyset_{j_k} \times \Delta r$$

(12)

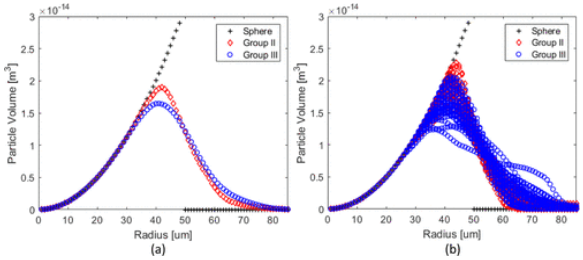

Figure 7. Particle volume distribution as a function of radius: (a) averaged data and (b) individual data.

Plotting volume distributions, rather than just macroporosity distributions (which are shown in Figure 8), is informative because the volume depends on both the surface fraction at a given radial

position as well as the radius at which the surface fraction was measured. Plotting macroporosity versus radius omits the importance of the area over which the surface fraction is calculated.

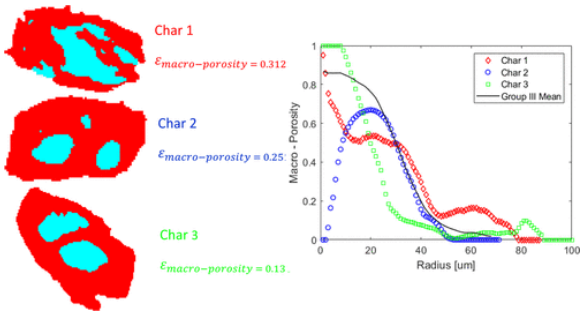

Figure 8. Three char particle cross sections and corresponding 3-D macroporosity distributions collapsed to 1-D.

It can be seen from Figure 7a that the average particle volume distribution matches that of a perfect sphere for radii smaller than 26 µm and is approximately the same as that of a spherical particle up to radii of 40 µm. As expected, group II particles are more spherical than their group III counterparts,[7] as their average volume distribution deviates from the sphere's volume at larger radii. Although there is a clear difference when comparing the average particle radial distributions, the individual data in Figure 7b show that some group III particles follow the same volume distribution as group II particles, although the denser group III particles have a broader range of particle volume distributions, indicating more irregularity in their shape, and causing the mean distribution of group III particles to be less spherical.

As mentioned above, at approximately 40 µm, the particle volume distribution begins to deviate from that of a perfect sphere, which indicates that surrounding fluid occupies some of these regions. This implies that particle regions beyond 40 µm from the particle's center are increasingly likely to be protrusions with enhanced accessibility to gas-phase reactants. The exposure of the protrusion's external surface to the bulk gases will lower the diffusion length scales for the microporous solid within the protrusions, increasing their internal reactant concentrations and increasing char conversion rates. This may have been a contributing factor in the pore-resolving CFD study by Fong et al.,[36] in which higher reactant concentrations were observed within the microporous solid for a 3-D resolved char particle compared to a perfectly spherical particle.

The macroporosity distribution as a function of radius is shown in Figure 8 for three individual char particles, with corresponding cross sections that intersects their center of microporous solid volume also shown. The macroporosity at each radius, *k*, is calculated using eq 13 which has been simplified from eq 1a using eq 12, yielding the macroporosity at a given radius in terms of the surface fractions.

$$\varepsilon_{\text{macro-pore}_k} = \frac{\text{Ø}_{\text{macro-pore}_k}}{\left(\text{Ø}_{\text{microporous solid}_k} + \text{Ø}_{\text{macro-pore}_k}\right)} \quad (13)$$

The mean macroporosity distribution for group III particles is also shown in Figure 8. Because macroporosity is only defined within the particles, the mean distribution ceases once the first particle

of the group has been fully encapsulated by the sphere used to determine surface fraction, as this causes the denominator in eq 13 to be zero for that particle.

Although the macropores for the three individual particles appear to be randomly dispersed throughout the char, when the 3-D measurements are collapsed to 1-D, centrally located macropores can be observed for char 1 and char 3. The macroporosity exhibits a peak at approximately 20 µm for char 2. For all three chars, nonmonotonicity in the macroporosity as a function of radius is observed, whereas the group III mean exhibits a nearly monotonic decrease in macroporosity with radius.

The mean macropore volume distribution and mean macroporosity distribution for both groups are plotted in Figure 9a,b, respectively. It is observed in Figure 9a that group II particles have a higher macropore volume and macroporosity for all radii, as expected, because this group has, by definition, the larger total macroporosity. Also, a trend of decreasing macroporosity with increasing distance from the particle's center is observed for both particle groups. Figure 9a,b shows that the macropores are centrally concentrated, which means that the microporous solid is preferentially located toward the particle's edge for both group II and III chars.

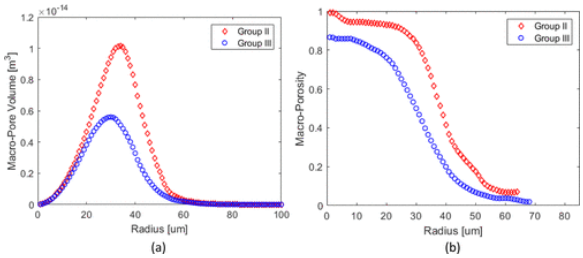

Figure 9. (a) Average macropore volume as a function of radius and (b) average macroporosity as a function of radius.

The adherence to a similar trend for both groups, but with different magnitudes of macroporosity, suggests the possibility that all of the char particles being examined might be represented by a single macroporosity distribution with radius. This was tested by normalizing the macroporosity and microporous solid curves such that all particles had an identical total macroporosity of 50%. Only the macroporosity versus radius is presented in Figure 10 because scaling can create nonrealistic macropore volumes.

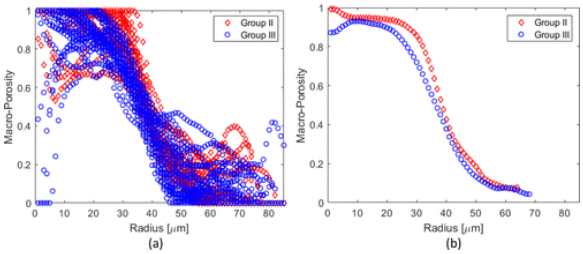

Figure 10. Scaled macroporosity as a function of radius: (a) individual particles, (b) averaged data for each group.

The scaled macroporosity is presented for every individual particle in Figure 10a. Most particles follow a similar trend and exhibit significant variation of normalized porosity with radius. Upon scaling, the mean macroporosity distribution for both particle groups nearly collapses to a single line, as shown in Figure 10b. The radial dependence of macroporosity demonstrates that, in the mean, even group III

char particles with lower macroporosity resemble a hollow sphere, rather than a solid particle with uniformly dispersed macropores. Classifying a broader distribution of char morphologies as hollow spheres with a range of wall thicknesses could reduce the complexity of char distribution models within CFD codes. However, whether representing a distribution of morphologies by its mean morphology (hollow sphere) accurately captures the combustion behavior of the distribution remains an open question. Because 3-D analysis of char morphology and macroporosity distributions has not been previously reported, the suitability of employing a hollow sphere structure for a range of coals and pyrolysis conditions would also require further investigation.

A critical step in employing a hollow sphere model for use in CFD codes would be the ability to characterize the distribution of char particle wall thicknesses using easily measurable characteristics. The theoretical wall thickness for a single hollow sphere (cenosphere) can be calculated using the total macroporosity and the outer radius, beginning with an equation for the total particle volume

$$\frac{4}{3}\pi r_{\text{outer}} = V_{\text{macro-pore}} + V_{\text{micro-porous solid}} \tag{14}$$

Equation 1a is then solved for $V_{\text{microporous solid}}$ and substituted into eq 14, to yield

$$V_{\text{macro-pore}} = \frac{\frac{4}{3}\pi {r_{\text{outer}}}^3}{1 + \frac{1 - \varepsilon_{\text{macro-pore}}}{\varepsilon_{\text{macro-pore}}}} \tag{15}$$

For a hollow sphere, $V_{\text{macropore}}$ can also be expressed by eq 16, as there is only a single, centrally located macropore

$$V_{\text{macro-pore}} = \frac{4}{3}\pi {r_{\text{inner}}}^3 \tag{16}$$

Equating eqs 15 and 16, r_{inner} can be obtained and substituted into the wall thickness equation, eq 17, to yield eq 18, which determines the microporous solid wall thickness using only total macroporosity and particle radius.

$$t_{\text{micro-porous solid}} = r_{\text{outer}} - r_{\text{inner}} \tag{17}$$

$$t_{\text{micro-porous solid}} = r_{\text{outer}} - \left(\frac{{r_{\text{outer}}}^3}{1 + \left(\frac{1 - \varepsilon_{\text{macro-pore}}}{\varepsilon_{\text{macro-pore}}} \right)} \right)^{1/3}$$

(18)

The accuracy of this approach can be evaluated by comparing the theoretical microporous solid thickness from eq 18 with the measured wall thicknesses, as described in Section 2.2.2. The average microporous solid thickness for each cross section is averaged to give a single measurement and is shown in Figure 11a for every particle studied. The average microporous solid thickness for each of the three cross sections is shown in Figure 11b for every particle. The theoretical wall thickness for a cenosphere is also shown in Figure 11a,b with a solid line. The measured wall thicknesses agree reasonably well with the theoretical hollow sphere approach for roughly 80% of the particles studied, with an average relative error of 10.0%.

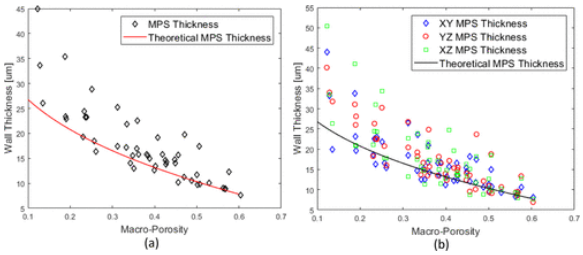

Figure 11. (a) Average microporous solid thickness as a function of macroporosity, and (b) average cross-sectional microporous solid thickness as a function of macroporosity.

The mean 3-D macropore distributions, together with the prediction of microporous solid wall thickness based solely on macroporosity, lend support to modeling these Illinois #6 chars as hollow spheres with a distribution of wall thicknesses rather than solid spheres with uniformly dispersed porosity. The wall thicknesses that fall further from the theoretical line in Figure 11a likely result from char particles with significantly nonuniform structures.

In the mean, these bituminous coal char particles were shown to have a cenospheric structure with varying wall thickness which can be estimated using a theoretical equation based on micro-CT measurements of particle macroporosity and radius. The “microporosity” of the solid regions, which is required for pore evolution and intrinsic reaction models, can be obtained from gas adsorption experiments, with all pore sizes below the micro-CT resolution associated with the microporosity.

In order to use this model, two assumptions about char morphology would need to be made. The first is that the char particle is spherical, which will cause an under-prediction of diffusion lengths and reaction rates if the particle has protrusions, as observed for these chars. The validity of this assumption can be quantified by measuring the sphericity of the char particle. The second assumption is that all microporous solid is located within the particle’s spherical shell, which is supported by the similar macropore radial distributions among a large range of char macroporosities. However, this is not completely accurate, as it was shown in Figures 8–10 that some char particles have a portion of their microporous solid centrally located. It is again emphasized that the accuracy of representing a distribution of morphologies by its mean morphology (hollow sphere) in modeling the combustion behavior requires further investigation.

Estimation of a particle’s macroporosity based on 2-D cross sections (the area estimation method of eq 1b) is the standard technique for characterization of morphological distributions,[3,19,20,22−31] but the

accuracy of this technique has not been assessed. The standard area estimation method and the proposed cylindrical stacking estimation method described in Section 2.2.3were therefore compared to the true macroporosity, calculated using 3-D volumes, as also described in Section 2.2.3. Three orthogonal cross sections that intersect the particle's microporous solid center of volume are employed for the approximate 2-D methods, so macroporosity is taken as an average of three area estimations or six cylindrical stacking measurements. Both 2-D techniques are compared to the true 3-D macroporosity in Figure 12. The cylindrical stacking method is more accurate in estimating the particle's macroporosity than the standard area estimation method. The difference between the true macroporosity and the corresponding estimated macroporosity is used to determine the absolute error. The average absolute error is −0.105 for the area estimation method and 0.0421 for the cylindrical stacking method. There is little correlation between the macroporosity and error, so the accuracy of the approximate 2-D methods appears to be independent of the true macroporosity. It should be noted that the average difference from true macroporosity for the sampled char particles was large enough to reject the null hypothesis that estimation methods predicted the true macroporosity according to a two-tailed test with an alpha value equal to 0.005. It was thus concluded that neither method estimates true macroporosity. The improvement obtained by using the cylinder stacking method stems from utilizing available char and macropore "diameters" from the cross section to estimate volumes, eliminating the error of estimating volume ratios with area ratios. The standard area estimation method neglects useful data present in the cross-sectional images by only utilizing the bulk area fractions.

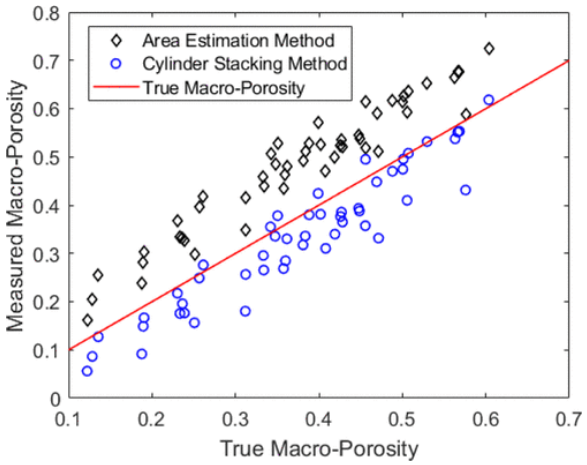

Figure 12. Measured macroporosity using 2-D methods compared to the true, 3-D macroporosity from micro-CT.

The accuracy of the 2-D estimation techniques is also expected to be somewhat inflated for the particles in this study, which are composed of a relatively large proportion of thin and thick-walled cenospheres, so the symmetric assumption employed in the area-based approaches is more realistic than they would be for other particles. Furthermore, the imaging planes used in this study were chosen to intersect the microporous solid's center of gravity, further improving the accuracy of the symmetric assumption for both 2-D methods, which will likely not be the case for most planes imaged for particles embedded in an epoxy resin. If a 2-D porosity estimation technique must be implemented, the cylindrical stacking method provides a more accurate estimation of total macroporosity. Nonetheless,

this technique is still subject to high variability when considering only a single char cross section because of a char's nonuniform morphology, as illustrated in Figure 1.

4. Conclusions

Micro-CT has been used, for the first time, to quantify morphological parameters, such as particle and pore volume, macroporosity, and wall thickness, for a distribution of pulverized coal char particles. The measured volumes and the macroporosity can be converted from 3-D maps to 1-D radial distributions using averaging over polar and azimuthal directions at each radial location. A technique for quantifying the average wall thickness for a char particle has been presented using micro-CT data, and a new method for estimating macroporosity using 2-D imaging, called the cylindrical stacking method, has been proposed for cases in which micro-CT imaging is not feasible. The analysis had been performed manually in this study, but it is possible that the process could be automated[37] to increase efficiency.

Using the proposed micro-CT analysis, a distribution of 50 pulverized bituminous coal char particles has been found to exhibit a similar spatial distribution of macroporosity across particles with widely varying total macroporosities, when appropriately normalized. For 80% of the particles imaged, the 3-D wall thickness measured by micro-CT was well predicted by a simple model representing the particles as thick- or thin-walled cenospheres. For these bituminous coal char particles, the separation of char particles into different morphological groups for simplified char particle combustion sub-models in CFD calculations may therefore be unnecessary, although this would require confirmation using particle-scale combustion simulations. Although such structure may exist in other coal chars with similar pyrolysis behavior, limitations in past image analysis techniques may have prevented this observation. This would have to be determined on a case-by-case basis for different coals and devolatilization conditions, but if applicable, the model reduces the number of parameters required to characterize a char particle's structure.

The principle limitations of 2-D approaches for particle classification and quantification are the use of a single cross-sectional image per particle, which results in inaccurate and biased predictions of macroporosity, as seen in Figure 12. The stark difference between 2-D and 3-D analyses revealed in this paper suggests that modifications to 2-D analyses are necessary, if they must be employed. To this end, a new 2-D approach for measuring macroporosity, called the cylindrical stacking method, was proposed and found to be more accurate than the standard area-based method when compared to the exact 3-D macroporosities obtained from micro-CT, reducing the error by 60% for the particles studied.

The authors declare no competing financial interest.

Acknowledgments

Acknowledgment is made to the donors of The American Chemical Society Petroleum Research Fund for support of this research. Images used courtesy of ANSYS, Inc. The authors thank April Neander and Prof. Zhe-Xi Luo at the PaleoCT Lab at the University of Chicago for micro-CT imaging.

References

1 Hecht, E. S.; Shaddix, C. R.; Molina, A.; Haynes, B. S. Effect of CO_2 gasification reaction on oxy-combustion of pulverized coal char. *Proc. Combust. Inst.* 2011, *33*, 1699– 1706, DOI: 10.1016/j.proci.2010.07.087

2 Dutta, S.; Wen, C. Y.; Belt, R. J. Reactivity of Coal and Char. 1. In Carbon Dioxide Atmosphere.*Ind. Eng. Chem. Process Des. Dev.* 1977, *16*, 20– 30, DOI: 10.1021/i260061a004

3 Liu, G.-S. Mathematical modelling of coal char reactivity in a pressurised entrained flow gasifier. Ph.D. Thesis, Department of Chemical Engineering, University of Newcastle, NSW, Australia, 1999.

4 Cloke, M.Characterization of coal with respect to carbon burnout in p.f.-fired boilers.*Fuel* 1997, *76*, 1257– 1267, DOI: 10.1016/s0016-2361(97)00016-1

5 Hodge, E. M.; Roberts, D. G.; Harris, D. J.; Stubington, J. F. The Significance of Char Morphology to the Analysis of High-Temperature Char–CO_2 Reaction Rates. *Energy Fuels*2010, *24*, 100– 107, DOI: 10.1021/ef900503x

6 Sahimi, M.; Gavalas, G. R.; Tsotsis, T. T. Statistical and Continuum Models of Fluid-Solid Reactions in Porous Media. *Chem. Eng. Sci.* 1990, *45*, 1443– 1502, DOI: 10.1016/0009-2509(90)80001-u

7 Yu, J.Formation of the Structure of Chars during Devolatilization of Pulverized Coal and Its Thermoproperties: A Review. *Prog. Energy Combust. Sci.* 2007, *33*, 135– 170, DOI: 10.1016/j.pecs.2006.07.003

8 Jones, R. B.; Morley, C.; McCourt, C. B. Maceral effects on the morphology and combustion of coal char. *Proceedings International Conference on Coal Science*, 1985; pp 669– 672.

9 Jones, R. B.; McCourt, C. B.; Morley, C.; King, K. Maceral and rank influences on the morphology of coal char. *Fuel* 1985, *64*, 1460– 1467, DOI: 10.1016/0016-2361(85)90351-5

10 Alvarez, D.; Menendez, R.; Fuente, E.; Vleeskens, J. Study of the influence of coal rank on char structure and behavior. *Seventh Conference Proceedings—International Conference on Coal Science*, 1993; pp 77– 80.

11 Oka, N.; Murayama, T.; Matsuoka, H.; Yamada, S.; Yamada, T.; Shinozaki, S.The influence of rank and maceral composition on ignition and char burnout of pulverized coal. *Fuel Process. Technol.* 1987, *15*, 213– 224, DOI: 10.1016/0378-3820(87)90046-4

12 Menéndez, R.; Vleeskens, J. M.; Marsh, H. The use of scanning electron microscopy for classification of coal chars during combustion. *Fuel* 1993, *72*, 611– 617, DOI: 10.1016/0016-2361(93)90572-j

13 Bailey, J. G.; Tate, A.; Diessel, C. F. K.; Wall, T. F. A char morphology system with applications to coal combustion. *Fuel* 1990, *69*, 225– 239, DOI: 10.1016/0016-2361(90)90179-t

14 Bend, S. L.; Edwards, I. A. S.; Marsh, H. The influence of rank upon char morphology and combustion. *Fuel* 1992, *71*, 493– 501, DOI: 10.1016/0016-2361(92)90145-e

15 Rosenberg, P.; Petersen, H. I.; Thomsen, E.; Thomsen, E.; Guvad, C. Combustion char morphology related to combustion temperature and coal petrography. *Fuel* 1996, *75*, 1071–1082, DOI: 10.1016/0016-2361(96)00074-9

16 Benfell, K. E.; Bailey, J. G. Comparison of combustion and high pressure pyrolysis chars from Australian black coals. *Eighth Australian Coal Science Conference Proceedings*, Sydney, Australia, 1998; pp 157– 162.

17 Lightman, P.; Street, P. J. Microscopical examination of heat treated pulverized coal particles. *Fuel* 1968, *47*, 7– 28

18 Littlejohn, R. F. Pulverized-fuel combustion: swelling under rapid heating. *J. Inst. Fuel* 1967,*40*, 128

19 Alvarez, D.; Borrego, A. G.; Menéndez, R. Unbiased methods for the morphological description of char structures. *Fuel* 1997, *76*, 1241– 1248, DOI: 10.1016/s0016-2361(97)00065-3
20 Cloke, M.; Lester, E. Characterization of coals for combustion using petrographic analysis: a review. *Fuel* 1994, *73*, 315– 320, DOI: 10.1016/0016-2361(94)90081-7
21 Vleeskens, J. M.; Menéndez, R. M.; Roos, C. M.; Thomas, C. G. Combustion in the burnout stage: the fate of inertinite. *Fuel Process. Technol.* 1993, *36*, 91– 99, DOI: 10.1016/0378-3820(93)90014-u
22 Cloke, M.Char Characterization and Its Application in a Coal Burnout Model. *Fuel*2003, *82*, 1989– 2000, DOI: 10.1016/s0016-2361(03)00155-8
23 Wu, T.A Burnout Prediction Model Based around Char Morphology. *Energy Fuels*2006, *20*, 1175– 1183, DOI: 10.1021/ef050101o
24 Ma, L.; Mitchell, R. Modeling Char Oxidation Behavior under Zone II Burning Conditions at Elevated Pressures. *Combust. Flame* 2009, *156*, 37– 50, DOI: 10.1016/j.combustflame.2008.06.015
25 Benfell, K. E.Modeling Char Combustion: The Influence of Parent Coal Petrography and Pyrolysis Pressure on the Structure and Intrinsic Reactivity of Its Char. *Proc. Combust. Inst.* 2000, *28*, 2233– 2241, DOI: 10.1016/s0082-0784(00)80633-5
26 Chaves, D.Automatic Characterisation of Chars from the Combustion of Pulverised Coals Using Machine Vision. *Powder Technol.* 2018, *338*, 110– 118, DOI: 10.1016/j.powtec.2018.06.035
27 Wu, T.Advanced Automated Char Image Analysis Techniques. *Energy Fuels* 2006,*20*, 1211– 1219, DOI: 10.1021/ef050360d
28 Lester, E.Char Characterization Using Image Analysis Techniques. *Energy Fuels*1996, *10*, 696– 703, DOI: 10.1021/ef9501713
29 Benfell, K. E. Assessment of char morphology in high pressure pyrolysis and combustion. Ph.D. Thesis, Department of Geology, University of Newcastle, 2001.
30 Wu, H. Ash formation during pulverised coal combustion and gasification at pressure. Ph.D. Thesis, Department of Chemical Engineering, University of Newcastle, Australia, 2000.
31 Zygourakis, K. Effect of Pyrolysis Conditions on the Macropore Structure of Coal-Derived Chars. *Energy Fuels* 1993, *7*, 33– 41, DOI: 10.1021/ef00037a007
32 Rouquerol, J.; Avnir, D.; Fairbridge, C. W.; Everett, D. H.; Haynes, J. M.; Pernicone, N.Recommendations for the characterization of porous solids (Technical Report). *Pure Appl. Chem.* 1994, *66*, 1739– 1758, DOI: 10.1351/pac199466081739
33 Mathews, J. P.; Campbell, Q. P.; Xu, H.; Halleck, P. A review of the application of X-ray computed tomography to the study of coal. *Fuel* 2017, *209*, 10– 24, DOI: 10.1016/j.fuel.2017.07.079
34 *Simpleware ScanIP Software*, Mountain View, CA, USA, 2017.
35 Fan, L. S.; Zhu, C. Size and Properties of Particles. *Principles of Gas–Solid Flows*;Cambridge University Press, 1998; pp 3– 45.
36 Fong, G. H.Pore-Resolving Simulation of Char Particle Gasification Using Micro-CT.*Fuel* 2018, *224*, 752– 763, DOI: 10.1016/j.fuel.2018.03.117
37 Ushizima, D.; Statistical segmentation and porosity quantification of 3D X-ray microtomography. *Proceedings SPIE 8135, Applications of Digital Image Processing XXXIV*, Sept 12, 2011; p 813502.